ЯДЕРНА ФІЗИКА
NUCLEAR PHYSICS

УДК 539.142+539.143.3 https://doi.org/10.15407/jnpae2025.02.113

A. A. Alzubadi*, R. T. Mahdi

Department of Physics, College of Science, University of Baghdad, Baghdad, Iraq

*Corresponding author: ali.abdullatif@sc.uobaghdad.edu.iq

INVESTIGATING NUCLEAR DEFORMATION AND LONGITUDINAL FORM FACTORS IN SOME *fp*-SHELL NUCLEI USING THE SHELL MODEL AND HARTREE - FOCK APPROXIMATION

The current study examined the nuclear deformation of certain Titanium and Chromium isotopes using the shell model and Hartree - Fock approximation within the *fp*-shell model space. The research calculated magnetic dipole and electric quadrupole moments, inelastic longitudinal Coulomb electroexcitation form factors, and low-lying excitation energies. The one-body transition density matrix elements for each transition in the *fp*-shell model space were computed using the FPD6 two-body effective interaction. The impact of varying the single-particle nuclear potentials, such as a harmonic oscillator, Woods - Saxon, and Skyrme - Hartree - Fock, was investigated in comparison with experimental data. Discrepancies with the experimental data led to adjustments in the two-body effective interactions or the model for calculating the effective charge of the nucleus for specific transitions. Furthermore, the study analyzed the potential energy surface and nuclear density distribution as a function of the quadrupole deformation parameter β_2 using the Hartree - Fock + Bardeen - Cooper - Schrieffer method.

Keywords: shell model, *fp*-shell model space, Skyrme - Hartree - Fock, quadrupole deformation parameters, Hartree - Fock + Bardeen - Cooper - Schrieffer.

1. Introduction

The nuclear shell model (SM) has proven to be a valuable tool in the exploration of nuclear structure. By carefully selecting appropriate residual effective interactions, it has been possible to accurately and consistently replicate various observables [1, 2]. Although relatively straightforward, the SM adeptly elucidates several nuclear phenomena, including spin, magnetic moment, and nuclear spectra. The choice of residual effective interactions is crucial and is determined by several significant factors. In the SM, effective interactions are influenced by nucleon-nucleon interactions derived from fundamental concepts such as quantum chromodynamics. Configuration mixing is a critical aspect because, in the model, multiple nucleons in different configurations must often be included to accurately describe nuclear correlations [3, 4].

The *fp*-shell is an interesting region for SM calculations that can be investigated by inelastic electron scattering, where the nucleus is considered to be inert ^{40}Ca, and the full $1f_{7/2}$, $2p_{3/2}$, $1f_{5/2}$, $2p_{1/2}$ space is used for valance nucleons. Electromagnetic observables provide helpful information for studying the structure of nuclei of both ground states and excited states. Specifically, it is projected that observables such as electric quadrupole ($E2$) transitions and quadrupole ($Q2$) moments will give accurate information about deformations [5 - 9]. The evolution mechanism of deformation will change the shapes of nuclei from the beginning to the end of the closed shell. Until now, the mass number dependence of the deformations has been examined mainly in nuclei. However, it is rather difficult in rare-earth and heavy nuclei to systematically analyze the deformations between two closed shells due to the limited available nuclei for experiments [10]. On the other hand, the closed shell may be accessed experimentally from beginning to end in *sd*- and *pf*-shell nuclei. Thus, the *sd*- and *fp*-shell nuclei may be good candidates to examine the dynamical development of deformation because multiple electric quadrupole transitions have previously been detected [11], and new information on unstable nuclei becomes available [12]. G. Mukherjee and S.K. Sharma [13] provided the form factors for the inelastic electron scattering to 2^+, 4^+, and 6^+ states in ^{46,48,50}Ti, ^{50,52,54}Cr, and ^{54,56}Fe isotopes within the framework of the projected Hartree - Fock - Bogoliubov wave functions. The results exhibited a good agreement with experimental form factors, using constant effective charges and no adjustable parameters for the calculations [13, 14]. Furthermore, A.A. Alzubadi et al. demonstrated that including the harmonic oscillator (HO) and Skyrme - Hartree - Fock (SHF) as residual interactions in the *p*-shell, *sd*-shell, and *fp*-shell are crucial for improving the calculations of the form factors [15 - 18].

This study examines the dynamic changes in nuclear deformation in the full *fp*-shell model space

© The Author(s), 2025
Published by INR of NAS of Ukraine as an open access article under the CC BY-NC 4.0 license

for Titanium and Chromium isotopes in two scenarios. In the first scenario, the SM utilized FPD6 two-body effective interaction and various single-particle potentials. The second scenario involved studying the quadrupole deformation parameter β_2 as a function of energy using the Hartree - Fock (HF) + Bardeen - Cooper - Schrieffer (BCS) method, which considers the nucleons' collective motion, which is not considered in the nuclear SM.

2. Theoretical framework

This section describes two types of formalism for calculations used in the present work: the SM calculations and the HF + BCS approximation.

2.1. SM calculations

The electromagnetic nuclear matrix element $\left(\hat{O}\right)$ can be described as the sum of the products result of the one-body density matrix (OBDM) and the single-particle matrix elements [19]

$$\left\langle f\left\|\hat{O}(\lambda)_{t_z}\right\|i\right\rangle = \sum_{k_a k_b}\mathrm{OBDM}\left(fik_ak_b\lambda\right)\left\langle k_a\left\|\hat{O}(\lambda)_{t_z}\right\|k_b\right\rangle. \tag{1}$$

The OBDM is given by

$$\mathrm{OBDM}\left(fik_ak_b\lambda\right) = \frac{\left\langle f\left\|a^{+}_{ka}\otimes\tilde{a}_{\mathrm{kb}}\right\|i\right\rangle}{\sqrt{2\lambda+1}}, \tag{2}$$

i and f encompass all the quantum numbers required to differentiate the states.

The nuclear magnetic dipole moment is described based on the $M1$.

$$\mu_{Th} = \sqrt{\frac{4\pi}{3}}\begin{pmatrix} J & 1\ J \\ -J & 0\ J\end{pmatrix}\sum_{t_z}\left\langle f\left\|\hat{O}(M1)_{t_z}\right\|i\right\rangle_{\mu_N}, \tag{3}$$

the nuclear magneton μ_N is equal to $\mu_N = \dfrac{eh}{2m_pc}$ which is equivalent to 0.1051 e·fm.

The electric quadrupole moment is determined with reference to the $E2$ operator

$$Q_{Th} = \sqrt{\frac{16\,\pi}{5}}\begin{pmatrix} J & 2\ J \\ -J & 0\ J\end{pmatrix}\sum_{t_z}\left\langle f\left\|\hat{O}(E2)_{t_z}\right\|i\right\rangle e_{t_z}, \tag{4}$$

where both initial and final nuclear states $|J\rangle$ contain all the necessary quantum numbers to differentiate between the nuclear states.

The Skyrme potential, denoted as V_{Skyrme}, is a two-body interaction for the central potential. In the HF approximation, generating a one-body potential from it is possible. This mean-field potential is supposed to represent the average influence of all the nucleons within the nucleus. It is used to approximate the realistic nucleon-nucleon (and nucleon-nucleon-nucleon) forces [20].

$$V_{Skyrme}\left(\vec{r}_1,\vec{r}_2\right) = t_0\left(1+x_0\hat{p}_\sigma\right)\delta_{12} + \frac{t_1}{2}\left(1+x_1\hat{p}_\sigma\right)\left[\vec{k}'^2\delta_{12}+\vec{k}^2\delta_{12}\right]+$$

$$+t_2\left(1+x_2\hat{p}_\sigma\right)k'\delta_{12}k + \frac{t_3}{6}\left(1+x_3\hat{p}_\sigma\right)p^\alpha\left(\frac{\vec{r}_1-\vec{r}_2}{2}\right)\delta_{12} + iW_0\vec{k}'\delta_{12}\left(\hat{\sigma}_1+\hat{\sigma}_2\right)\cdot\vec{k}+$$

$$+\frac{t_e}{2}\left(\left[3\left(\hat{\sigma}_1\cdot\vec{k}'\right)\left(\hat{\sigma}_2\cdot\vec{k}'\right)-\left(\hat{\sigma}_1\cdot\hat{\sigma}_2\right)\vec{k}'^2\right]+\delta_{12}\left[3\left(\hat{\sigma}_1\cdot\vec{k}\right)\left(\hat{\sigma}_2\cdot\vec{k}\right)-\left(\hat{\sigma}_2\cdot\vec{k}\right)\vec{k}^2\right]\right)+$$

$$+t_0\left[3\left(\hat{\sigma}_1\cdot\vec{k}\right)\delta_{12}\left(\hat{\sigma}_2\cdot\vec{k}'\right)-\left(\hat{\sigma}_1\cdot\hat{\sigma}_2\right)\vec{k}'\delta_{12}\vec{k}'\right], \tag{5}$$

where $\delta_{12}=\delta\left(\vec{r}_1-\vec{r}_2\right)$ and k,k' serve as the relative momentum operators, with k acting on the right and k' is the operator acting on the left, as defined by

$$\hat{k} = \frac{1}{2i}\left(\vec{\nabla}_1-\vec{\nabla}_2\right),\ \hat{k}' = \frac{1}{2i}\left(\vec{\nabla}_1-\vec{\nabla}_2\right) \tag{6}$$

and $\hat{P}_\sigma$ is the spin-exchange operator that is given as

$$\hat{P}_\sigma = \frac{1}{2}\left(1+\vec{\sigma}_1\cdot\vec{\sigma}_2\right). \tag{7}$$

The Coulomb form factor, which is longitudinal $F(C\lambda, q, f, i)$, refers to the electroexcitation form factors for elastic and inelastic scattering. The transverse electric $F(E\lambda, q, f, i)$ and transverse magnetic $F(M\lambda, q, f, i)$ form factors, with λ representing the multipolarity [21]. The final two form factor types can be categorized by the convection currents, with λ_c resulting from the nucleons' orbital motion and λ_m from the nucleons' magnetic moments. Hence, the overall longitudinal form factor can be expressed as

$$\left|F_C\left(q,f,i\right)\right|^2 = \sum_{\lambda\geq 0}\left|F\left(C\lambda\ ,q,f,i\right)\right|^2 \tag{8}$$

and the total transverse form factor as

$$\left|F_T(q,f,i)\right|^2 = \sum_{\lambda>0}\left\{\left|F(E\lambda,q,f,i)\right|^2 + \left|F(M\lambda,q,f,i)\right|^2\right\}. \quad (9)$$

The form factor for electroexcitation, which considers both angular momentum and momentum transfer q, between initial (i) and final (f) nuclear SM states, can be expressed as [22].

$$\left|F(\eta\lambda,q)\right|^2 = \\ = \frac{4\pi}{Z^2(2J_i+1)}\left|\left\langle f\left\|\hat{T}(\eta\lambda,q)\right\|i\right\rangle F_{c.m.}(q)F_{f.s.}(q)\right|^2, \quad (10)$$

where η represents the longitudinal and transverse form factors, which are also known as Coulomb C. The finite size (*f.s.*) nucleon form factor superscript accounts for the absence of translational invariance in the SM. The mass number is represented by A, while the HO size parameter is denoted by b.

2.2. HF + BCS calculations

The self-consistent mean field method combines HF + BCS calculations to analyze nuclear structure and investigate deformation shapes. Considering the pairing correlation, this method utilizes Skyrme forces to study the transitional density shape. The HF method is regarded as the most effective technique for predicting the individual energy levels of closed-shell nuclei [23]. The SHF method is also advantageous due to its central force and interactions with zero range [24, 25]. Nuclei is a quantum many-body system that exhibits quadrupole collectivity associated with the mean-field shape. The collective degree of freedom is related to the measure of the operator $\hat{Q}$.

The building block of a mean-field theory is a set of single-particle wave functions ψ_α together with fractional occupation amplitudes υ_α i.e. [26] $\{\varphi_\alpha, v_\alpha, \alpha = 1,\ldots,\Omega\}$, Ω represents the active single-particle space size and the occupation amplitudes are restricted to the range $0 \le \upsilon_\alpha \le 1$.

The BCS is the complementary non-occupation amplitude, with the many-body state being made up of these components [26].

$$|\phi\rangle = \prod_{\alpha>0}\left(u_\alpha + v_\alpha \hat{a}^+_\alpha \hat{a}^+_{\bar{\alpha}}\right)|0\rangle, \quad (11)$$

where $|0\rangle$ represents the state of a particle in a vacuum, $\hat{a}^+_\alpha$ stands for the creation operator of a Fermion in the ψ_α, and $\bar{\alpha}$ the time-reversed counterpart of the state. The local nucleon density α is characterized as [26]

$$\rho_q(\vec{r}) = \sum_{\alpha\in q}\sum_s v^2_\alpha \left|\psi_\alpha(\vec{r},s)\right|^2. \quad (12)$$

The total energy is composed as

$$E_{tot} = T + E_{Skyrme} + E_{Coulomb} + E_{pair} + E_{c.m}, \quad (13)$$

where E_{Skyrme} - Skyrme energy, $E_{Coulomb}$ - Coulomb energy are given by [26]

$$E_C = \frac{e^2}{2}\int dV dV' \frac{\rho_p(\vec{r})\rho_p(\vec{r}')}{|\vec{r}-\vec{r}|} - \int dV \frac{3e^2}{4}\left(\frac{3}{\pi}\right)^{\frac{1}{3}}\rho_p^{4/3} \quad (14)$$

and the pairing energy is

$$E_{pair} = \frac{1}{4}\sum_{q\epsilon\{p,n\}} V_{pair,q}\int dV\left|\xi_q\right|^2\left[1-\frac{\rho}{\rho_{0,pair}}\right], \quad (15)$$

where dV represents the volume element throughout the three-dimensional space, e is the elementary charge with e^2 equal to 1.43989 MeV·fm, and ξ_q is the pairing density [26]

$$\xi_q = \sum_{\alpha\in q}\sum_s w_\alpha u_\alpha v_\alpha \psi_{\bar{\alpha}}(\vec{r},s)\psi_\alpha(\vec{r},s), \quad (16)$$

where w_α represents a soft cut-off of pairing space. The $s\ \epsilon \pm 1$ variables indicate the spinor part of the wave functions. The pairing energy includes the parameter ρ_0, a *pair* that regulates the balance between volume and surface pairing. Nuclear deformation is described as the deviation from the spherical symmetry around the center of mass (cm), which is indicated by the electric quadrupole moment. Therefore, the center of mass moments are the most crucial moments [26]

$$\vec{R}_{type} = \frac{\int dV\vec{r}\,\rho_{type}(\vec{r})}{\int dV\rho_{type}(\vec{r})}, \quad (17)$$

where "*type*" may denote proton ρ_p, neutron ρ_n isoscalar, or total from the total density $\rho = \rho_p + \rho_n$ or isovector moment from the isovector density

$$\rho_{T=1} = \frac{N}{A}\rho_p - \frac{Z}{A}\rho_n. \quad (18)$$

The anisotropic mixtures can be measured using the spherical quadrupole moments [26]

$$Q_{2m,type} = \int dV r^2 Y_{2m}\rho_{type}(\vec{r}-\vec{R}_{type}). \quad (19)$$

Axial symmetry permits non-vanishing quadrupole moments only $m = 0$. It is often convenient to express

them as a dimensionless quadrupole moment (quadrupole deformation parameter)

$$\beta_{20} = \frac{4\pi}{3}\frac{Q_{20}}{AR^2}, \quad R = R_0 A^{1/3}, \quad R_0 = 1.2\,\text{fm} \qquad (20)$$

every wave function and field is specified on a grid based on axial coordinates. The relationship between axial coordinates and Cartesian coordinates is explained

$$r = \sqrt{X^2 + Y^2}, \quad Z = Z, \qquad (21)$$

where r represents the axial coordinate that indicates the space point's distance from the symmetry axis. Objects that exhibit axial symmetry, such as densities and potentials, are only dependent on the r and z axes. r and z are both depicted on a central grid

$$r \leftrightarrow \left\{r_0, \ldots, r_{N_r}\right\}, \quad r_v = v\Delta r, \qquad (22)$$

$$z \leftrightarrow \left\{\left(z_{-N_z} \ldots, z_{-1}\right), z_0, \ldots, z_{N_z}\right\}, z_v = v\Delta z, \qquad (23)$$

where Δr and Δz are numerical parameters used to determine the grid spacing. Along the z-axis, the filled grid from $-N_z$ to $+N_z$ allows reflection-asymmetric nuclear configurations or from 0 for $+N_z$ and utilizes reflection symmetry to reconstruct the entire grid. Densities and potentials are axially symmetric functions $f(r, z)$ and trivially represented as $f(r_{vr}, z_{vz})$ on the grid. A wave function of a single particle presents a more complex composition including angular dependence and spin. It is illustrated as [26]

$$\psi_\alpha = \begin{pmatrix} \psi_\alpha^{(+)}\left(r_{v_r}, z_{v_z}\right)\exp\left(im_\alpha\phi\right) \\ \psi_\alpha^{(-)}\left(r_{v_r}, z_{v_z}\right)\exp\left(i(m_\alpha + 1/2)\phi\right) \end{pmatrix} \qquad (24)$$

the z-component of orbital angular momentum of the upper spin component is represented by m_α and with $K_\alpha = m_\alpha + 1/2$, it is the z-component of total z angular momentum.

3. Results of discussions

Our current study utilized the most recent NuSellX@MSU code [27] to compute the OBDM elements in the full *fp*-shell model space. This space includes the $1f_{7/2}$, $2p_{3/2}$, $2p_{1/2}$, and $1f_{5/2}$ valence orbitals with a ^{40}Ca nucleus serving as the inert core and FPD6 two-body effective interaction [28]. This interaction was employed within the full *fp*-shell model space to compute the OBDM elements. The FPD6 interaction, developed by W. Richter et al. [28], is a semi-empirical interaction constructed using a modified surface one-boson exchange potential framework. It incorporates central, spin-orbit, and tensor components, along with empirically fitted monopole core-polarization corrections. Additionally, we employed the HF + BCS code to analyze the β_2 as a function of energy. Our discussion of the results will be divided into four sections: the first section focuses on nuclear electromagnetic moments, followed by an examination of electroexcitation form factors. Followed by the excitation energies, and finally, we explore the β_2 parameter using the HF + BCS method.

3.1. The nuclear electromagnetic moments

The magnetic dipole μ_{Th} and electric quadrupole Q_{Th} moments are being calculated for Titanium and Chromium using the OBDM with a HO potential. The size parameters (b) of the HO are being calculated and selected based on the mass number (A) [29]

$$b = \sqrt{\frac{\hbar}{M_P\omega}}, \quad \hbar\omega = 45A^{-\frac{1}{3}} - 25A^{-\frac{2}{3}},$$

where M_P - mass of a proton.

In Table 1, the calculated μ_{Th} for selected Titanium isotopes are presented. The calculated magnetic moment for the excited 2^+ state (0.889 MeV) of ^{46}Ti is +0.668 nm, which is close to the experimental value of +0.99(5) nm but slightly lower [30]. This indicates that the model captures the general trend but may underestimate the dipole moment. The calculated μ_{Th} for the excited 2^+ state (0.984 MeV) of ^{48}Ti is +0.638 nm, closely matching the experimental value of +0.78(4) nm [30]. This indicates a similar trend as observed in ^{46}Ti. For ^{50}Ti, the calculated magnetic moment for the excited 2^+ state (1.554 MeV) is closer to the experimental value than the previous isotopes, indicating an improved prediction for ^{50}Ti.

Table 1. **The calculated magnetic dipole and electric quadrupole moments for Titanium isotopes in full *fp*-shell model space using FPD6 two-body effective interaction and compared with the results of experimental data [30]**

Isotopes ^{22}Ti A, N	J^π	b	E_x, MeV		μ, nm		Q, e·fm^2	
			Theo.	Exp.	Theo.	Exp.	Theo.	Exp.
46, 24	2^+	1.978	0.977	0.889	+0.668	+0.99(5)	–23.59	–21(6)
48, 26	2^+	1.989	1.177	0.984	+0.638	+0.78(4)	–18.87	–17.7(8)
50, 28	2^+	2.000	1.828	1.554	+2.270	+2.89(15)	+3.64	+8.0(16)

The quadrupole moments for the Titanium isotopes are shown also in Table 1. The most accurate results for isotopes ^{48}Ti and ^{46}Ti are –18.87 and –23.59 e·fm^2, respectively. These values match well with the experimental values of –17.7(8) and –21(6) e·fm^2 [30], and they indicate oblate deformation, showing that the model can predict deformation characteristics. However, the result for ^{50}Ti, which is +3.64 e·fm^2, does not match the experiment value and +8.0(16) e·fm^2 [30], suggesting prolate deformation and the breakdown of the magicity at $N = 28$ with the FPD6 interaction.

In Table 2 the values of μ_{Th} and Q_{Th} for selected Chromium isotopes are presented. The calculated magnetic moment for the excited 2^+ state (0.783 MeV) of ^{50}Cr is found to be +1.08 nm, close to the experimental value of +1.24(6) nm [30]. This indicates that the theoretical model used effectively reproduced the essential magnetic properties of ^{50}Cr. For the ^{52}Cr isotope, the calculated magnetic moment of the excited 2^+ state (1.434 MeV) is +1.897 nm, slightly lower than the experimental value of +2.41(13) nm [30], but still within the error margin. The larger uncertainty in the experimental measurement makes it difficult to draw a definitive conclusion, but the general agreement suggests that the model is reasonably accurate for this isotope. Finally, for ^{54}Cr, the calculated magnetic moment of the excited 2^+ state (0.835 MeV) is +1.109 nm which fairly matches the experimental value of +1.1(2) nm [30], showing the accuracy of the theoretical framework in predicting the magnetic dipole moment for this isotope.

Table 2. **The calculated magnetic dipole and electric quadrupole moments for Chromium isotopes in full fp-shell model space using FPD6 two-body effective interaction and compared with the results of experimental data [30]**

Isotopes ^{24}Cr A, N	J^π	b	E_x, MeV		μ, nm		Q, e^2·fm^2	
			Theo.	Exp.	Theo.	Exp.	Theo	Exp
50, 26	2^+	2.000	0.885	0.783	+1.08	+1.24(6)	–32.97	–36.0(7)
52, 28	2^+	2.011	1.592	1.434	+1.897	+2.41(13)	–20.08	–8.0(2)
54, 30	2^+	2.022	0.948	0.835	+1.109	+1.1(2)	–29.51	–21.0(8)

Table 2 presents the calculated results of the Q_{Th} for the Chromium isotopes. The result for the ^{50}Cr isotope is –32.97 e·fm^2, suggesting that the model accurately illustrates the deformation in this isotope, which is flattened along one axis (oblate deformation). The result for ^{52}Cr is –20.08 e·fm^2, significantly different from the experimental value of –8.0(2) e·fm^2. The result for ^{54}Cr is –29.51 e·fm^2, which falls within a reasonable range of uncertainty based on the experimental value of –21.0(8) e·fm^2. The full *fp*-shell model with the FPD6 interaction effectively describes the deformation characteristics of Titanium and Chromium isotopes, grabbing general trends and behaviors despite discrepancies in the exact values of quadrupole moments.

3.2. Inelastic electron scattering form factors

The study of inelastic electroexcitation form factors gives a full and detailed investigation of electromagnetic properties and the internal structure of the nuclei [31, 32]. This study takes into consideration a quite wide range of nuclear processes and applies different nuclear single-particle models such as SHF, HO, and Woods - Saxon (WS). Having performed such a comparison for Titanium and Chromium isotopes, we confirm the validity of the models and indicate what can be done to enhance them. In most cases studied, the shell-model version of the Bohr - Mottelson (BM) collective model was employed. This version utilizes microscopic collective models to derive the collective (rotational and vibrational) modes from the Schrödinger equation for the many-particle nuclear Hamiltonian, in contrast to the postulated modes in the phenomenological collective models.

The effective charges are formulated following BM [1] to explicitly include neutron excess and generally compensate for missing excitations beyond the limited model space via the relations $e_n^{BM} = e_{pol}$ and $e_p^{BM} = 1 + e_{pol}$, where the e_{pol} term is given by the following equation

$$e_{pol} = \\ = e\left\{Z/A - 0.32(N-Z)/A + \left[0.32 - 0.3(N-Z)/A\right]\tau_z\right\}.$$

3.2.1. Longitudinal *C*2 form factors

The forthcoming discussion will explore the impact of altering the nuclear single-particle potentials on the overall behavior of the inelastic nuclear form factors. This analysis aims to elucidate the extent to which these potentials can approximate the general behavior exhibited by the experimental data.

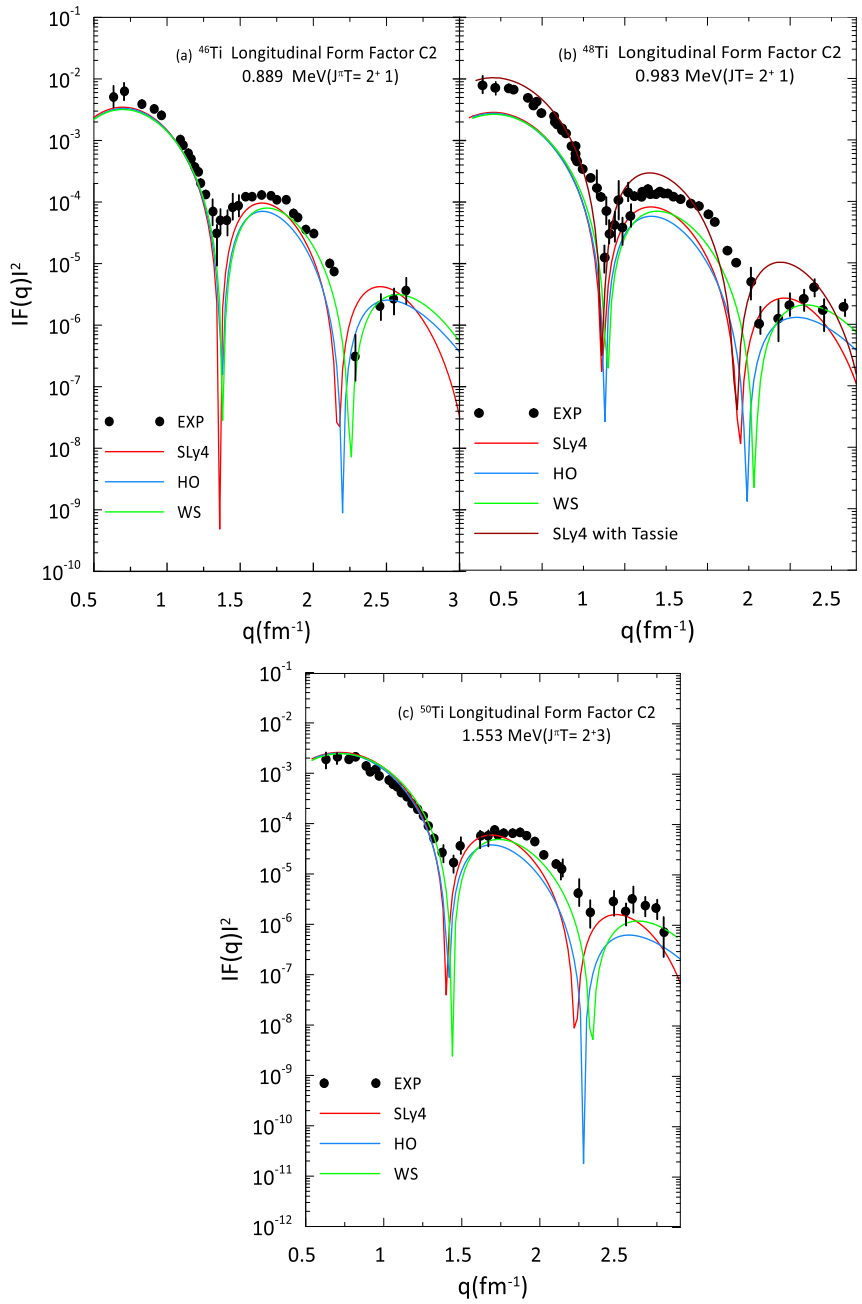

Fig. 1. Theoretical longitudinal $C2$ form factors of 2^+ transitions for: *a* - ^{46}Ti (0.889 MeV), *b* - ^{48}Ti (0.984 MeV), *c* - ^{50}Ti (1.554 MeV) using SLy4 parameterization, HO and WS compared with experimental data taken from Ref. [33]. (See color Figure on the journal website.)

Fig. 1 shows the calculated longitudinal $C2$ form factors for the transition to the low-lying excited state 2^+ in the ^{46,48,50}Ti isotopes with excitation energies of 0.889, 0.984, and 1.554 MeV, respectively. The form factor profile shows three peaks using the SLy4, HO, and WS potentials. The peak position and magnitude of experimental data [33] are successfully reproduced using the three potentials in the momentum transfer region up to 2 fm^{-1} without using any truncation to the SM space and adjustable parameters. Beyond that point, the deviation gradually increases due to the fluctuation of the experimental data, even with the theoretical form factors themselves. For more details, the SHF potential with SLy4 parametrization consistently provides the best agreement with the experimental data, indicating its robustness in predicting the inelastic longitudinal $C2$ form factors. The HO potential also performs well but shows increasing deviation with increasing the q values. The WS potential, although following the general trend, consistently shows the largest deviations, suggesting it may be less reliable for these transitions. In regard to the ^{48}Ti isotope, it is clear that the present calculations of the longitudinal $C2$ form factors are underestimating the experimental data across the entire momentum transfer region. This has prompted

us to consider improving the results by modifying the theoretical model using a single-particle nuclear potential that aligns with the experimental data, specifically the SHF with SLy4 parameterization potential. As shown in Fig. 1, *b*, the Tassie model [34] was employed to adjust the theoretical model, resulting in a positive impact on the convergence of the theoretical calculations with the experimental values for this particular isotope.

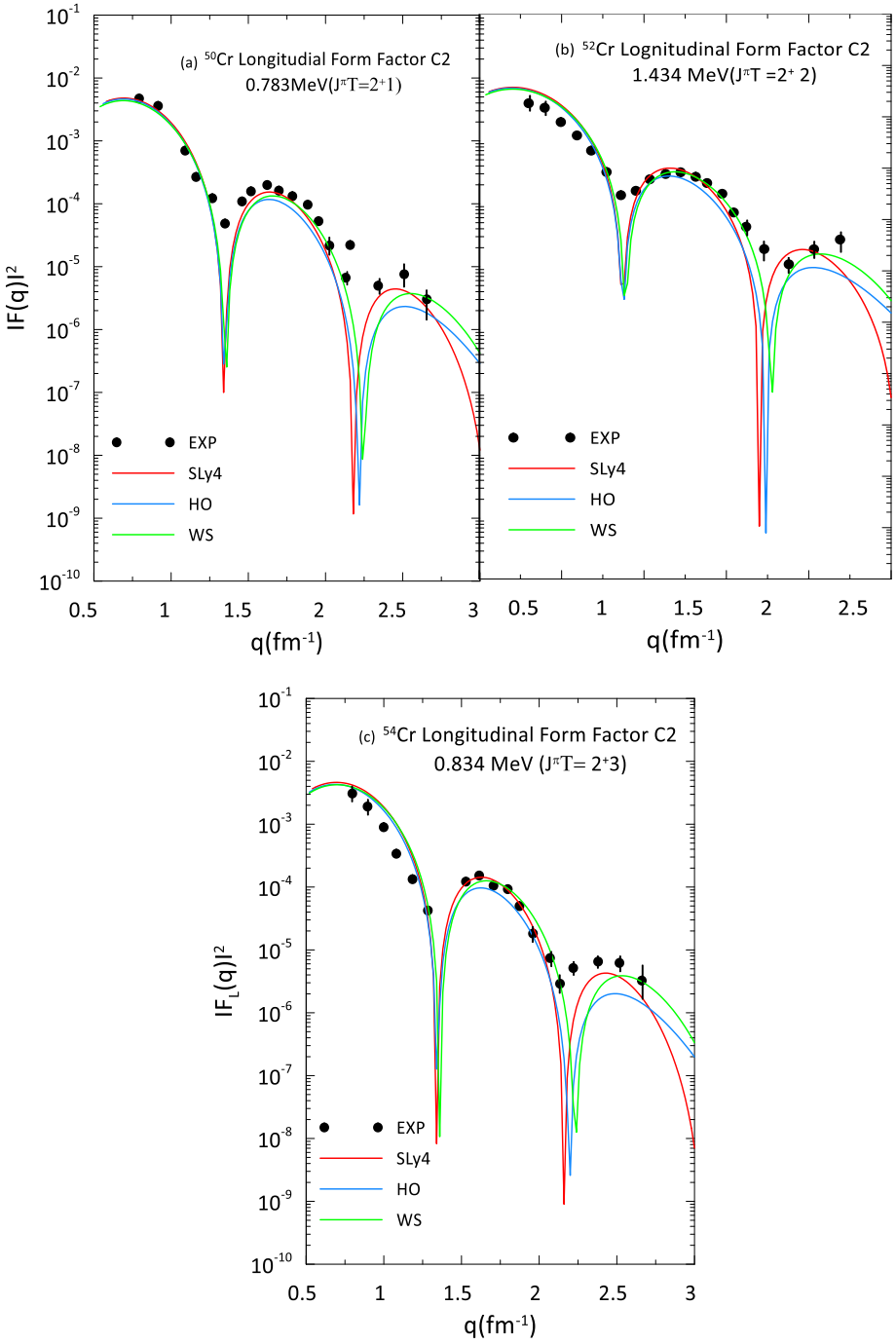

Fig. 2. Theoretical longitudinal $C2$ form factors of 2^+ transitions for: *a* - ^{50}Cr (0.783 MeV), *b* - ^{52}Cr (1.434 MeV), *c* - ^{54}Cr (0.834 MeV) using SLy4 parameterization, HO and WS compared with experimental data taken from Ref. [35]. (See color Figure on the journal website.)

The comparison in Fig. 2 presents the experimental data [35, 36] and theoretical longitudinal $C2$ form factors for the transition to the low-lying 2^+ excited state in the ^{50,52,54}Cr isotopes at excitation energies 0.783, 1.434, and 0.835 MeV, correspondingly. The first two peaks in all of these isotopes are accurately reproduced using full *fp*-shell model space. This indicates that the $C2$ form factors are satisfactorily replicated for the majority of nuclei in the *fp*-region when three potentials are applied to all the nuclei.

3.2.2. Longitudinal *C*4 form factors

Fig. 3 illustrates the theoretical longitudinal *C*4 form factors for 4^+ transitions in the ^{48,50}Ti isotopes at excitation energies of 2.295 and 2.674 MeV, respectively. Upon inspection of the calculated form factors profiles, it is evident that the experimental data were quite well reproduced using various single-particle potentials, SLy4, HO, and WS, although there is a slight deviation. Notably, the change in potentials does not significantly alter the general trend of the form factors in the full *fp*-shell model space. This overall agreement between the theoretical models and experimental data emphasizes the reliability of these parameterizations in modeling the *C*4 form factors for these isotopes.

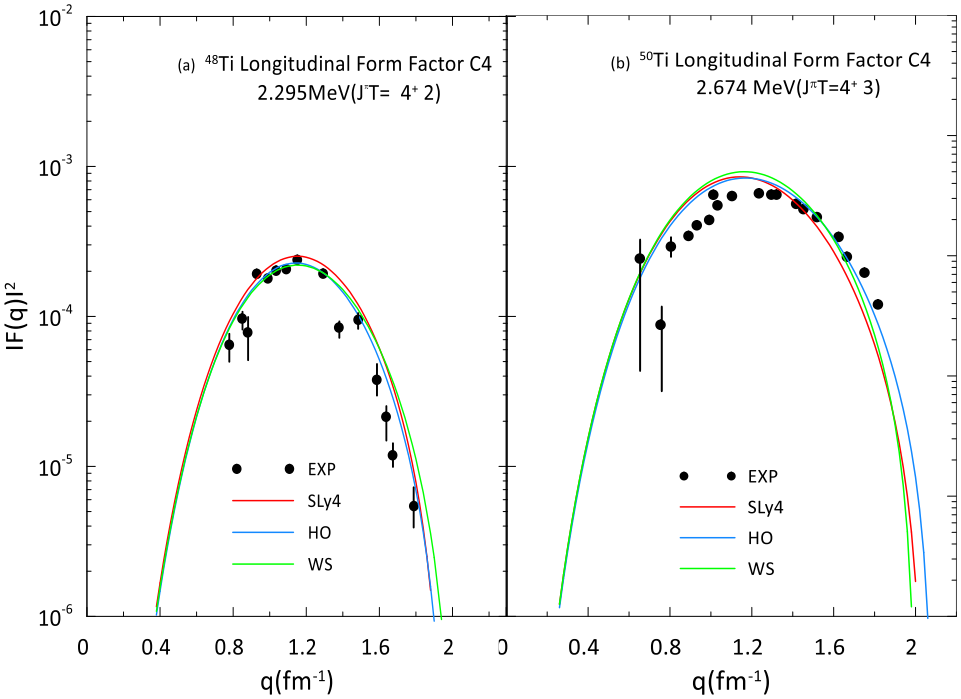

Fig. 3. Theoretical longitudinal *C*4 form factors of 4^+ transitions for: *a* - ^{48}Ti (2.295 MeV), *b* - ^{50}Ti (2.674 MeV), using SLy4 parameterization, HO and WS compared with experimental data taken from Ref. [36]. (See color Figure on the journal website.)

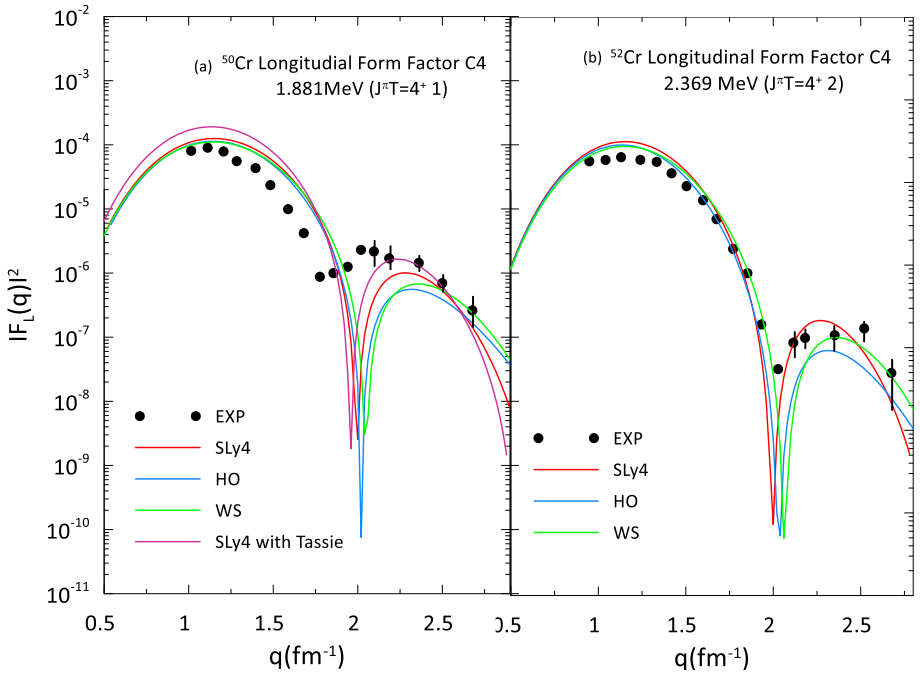

Continuation of Fig. 4

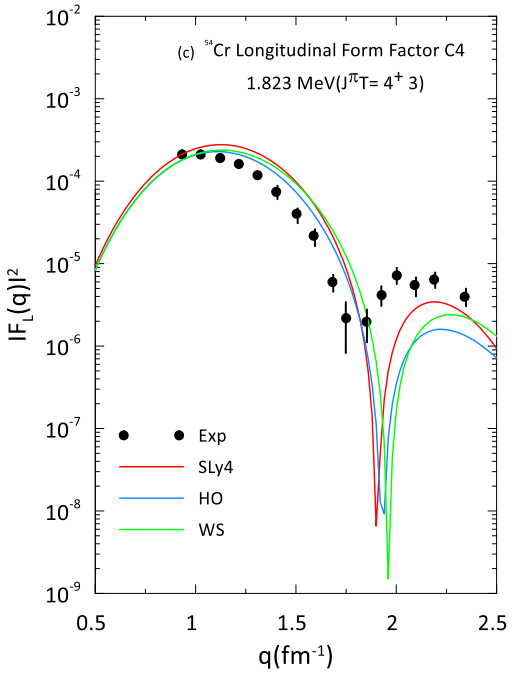

Fig. 4. Theoretical longitudinal $C4$ form factors of 4^+ transitions for transitions for: *a* - ^{50}Cr (1.88 MeV), *b* - ^{52}Cr (2.3697 MeV), *c* - ^{54}Cr (1.823 MeV) using SLy4 parameterization, HO and WS compared with experimental data taken from Ref. [35]. (See color Figure on the journal website.)

Fig. 4 shows the calculated and experimental longitudinal $C4$ form factors for the transition to the low-lying 4^+ excited state in ^{50,52,54}Cr isotopes at excitation energies of 1.881, 2.369, and 1.823 MeV, respectively. The form factor profiles exhibit two maxima for each isotope, which reasonably align with the experimental data. When examining the $C4$ form factor for ^{50}Cr, it is evident that the calculated results initially overestimate the experimental data up to 2 fm^{-1}, but this deviation gradually decreases and becomes underestimated. Despite attempting to adjust the model, agreement is only achieved in the high momentum transfer regions, with the agreement being restored when $q > 2.2$ using the Tassie model. The same trend was also observed for the other ^{52,54}Cr isotopes, showing a clear agreement with experimental data and a slight preference for SHF with SLy4. The SLy4 parameterization uses a specific set of parameters that effectively describe the nuclear structure and interactions. These parameters can be fine-tuned according to the specific properties of these isotopes, including nuclear density distribution and shell effects.

3.2.3. Longitudinal *C*6 form factors

In Fig. 5 the longitudinal $C6$ form factors for the transition to the low-lying 6^+ excited state in ^{50}Ti isotopes at excitation energies of 3.198 MeV are depicted. It is clear that all the potentials in the full *fp*-model space reasonably reproduced the general trend of the experimental data. Even the position of the maxima is reproduced rather well, although they exceed it.

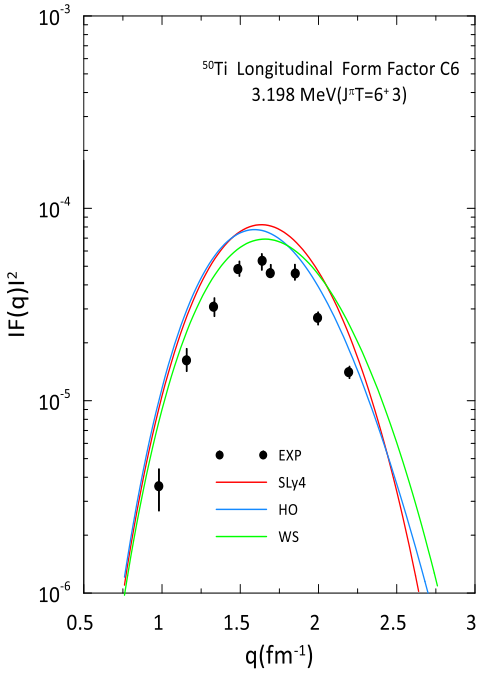

Fig. 5. Theoretical longitudinal $C6$ form factors of 6^+ transitions for transitions for ^{50}Ti (3.198 MeV) using SLy4 parameterization, HO, and WS compared with experimental data taken from Ref. [37]. (See color Figure on the journal website.)

The graph in Fig. 6 illustrates the longitudinal $C6$ form factors for the transition to the low-lying 6^+excited state in ^{50,52,54}Cr isotopes at excitation energies of 3.164, 3.113, and 3.222 MeV, respectively. In Fig. 6, *a*, the calculations for ^{50}Cr using full *fp*-model space with two-body matrix elements of the FPD6

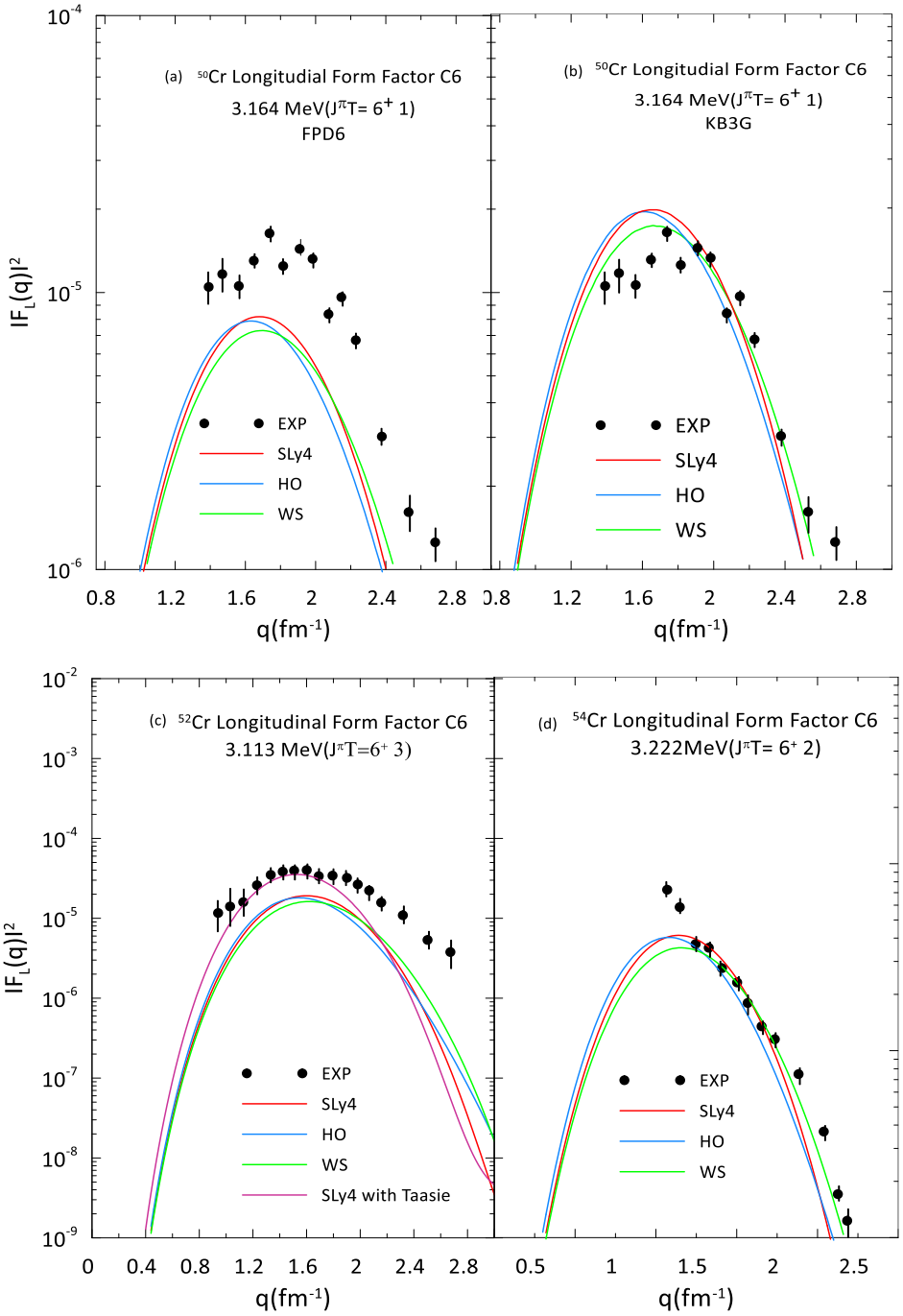

Fig. 6. Theoretical longitudinal *C*6 form factors of 6^+ transitions for: *a* - ^{50}Cr (3.16 MeV), *b* - ^{50}Cr (3.16 MeV) with KB3G, *c* - ^{52}Cr (3.113 MeV), *d* - ^{54}Cr (3.222 MeV) using SLy4 parameterization, HO and WS compared with experimental data taken from Ref. [35]. (See color Figure on the journal website.)

interaction were conducted. However, the model space failed to replicate the experimental data, and adjustments to the single-particle potentials did not lead to any improvement. Neither the BM model nor the FPD6 interactions precisely reproduced the longitudinal form factor profile despite the relatively small excitation energy. So, we have carried out the full *pf*-shell calculation with KB3G [38] two-body effective interaction to overcome this deviation with the experimental data. It is a new mass-dependent version of the FB3, the most frequently used effective interactions for the *pf*-shell model space. As shown in Fig. 6, *b*, this interaction yields a good agreement with the experimental data using the selected potentials. The agreement was also noticed in the *C*6 form factor in the ^{52}Cr isotope (see Fig. 6, *c*), particularly in the high momentum transfer region. We have also calculated the longitudinal *C*6 form factors for the ^{54}Cr isotope, as shown in Fig. 6, *c*. When using the Tassie model, we successfully reproduced the experimental *C*6 form factor in line with the data at $0.8 < q < 1.8$ fm^{-1}. However, discrepancies become more pronounced as the momentum transfer increases.

3.3. The excitation energies

The calculated low-lying positive parity excited states for the selected Titanium and Chromium isotopes are depicted in Figs. 7 and 8 using the entire *fp*-shell model space with FPD6 two-body effective interaction. The experimental levels are plotted on the left-hand panel with the line length proportional to the *J* value. If the *J* value is not specific, it is indicated by a point on the *y*-axis. The lines end in crosses for negative parity and filled circles for positive parity states. The theoretical results for positive parity states obtained in the *fp*-model space are shown on the right-hand panel. The correspondence between the calculated levels and the experimental data [39] is generally good, but there are slightly noticeable differences upon closer inspection. Across the different isotopes, the ordering of all the energy levels is predicted correctly. The slight deviations observed suggest areas where the model could be refined for improved accuracy. Overall, the comparisons demonstrate the effectiveness of the FPD6 interaction in capturing the essential features of nuclear excitation energies for these isotopes. This interaction uses a parameter set that accurately reflects the nuclear interactions and structure of the isotopes studied. This fine-tuning allows for precise predictions of excitation energies.

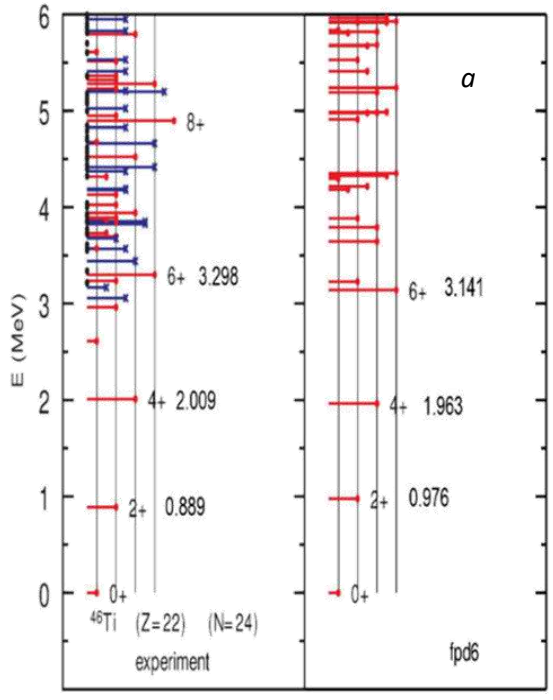

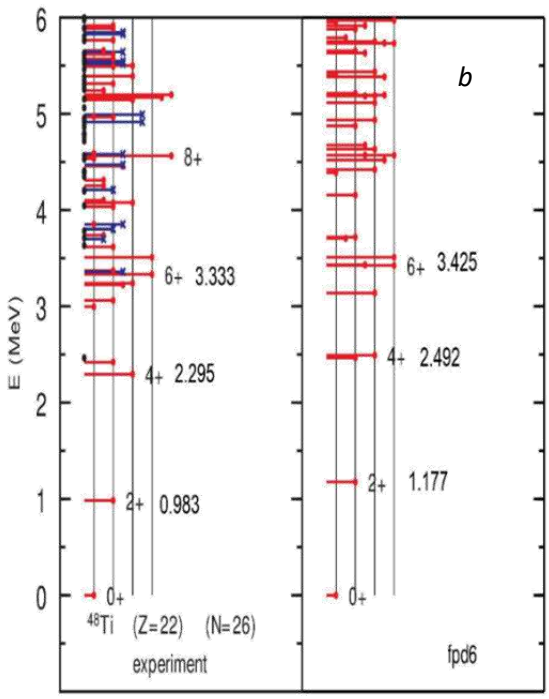

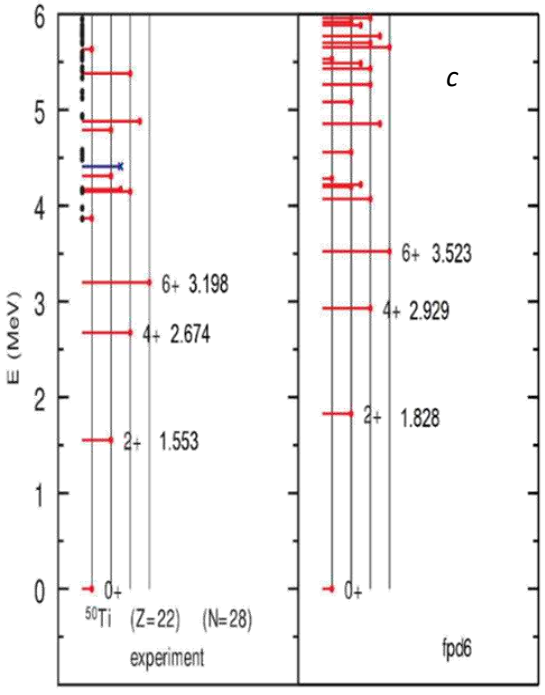

Fig. 7. Theoretical calculations of the low-lying positive parity excited states compared with the experimental data [39] for: *a* - ^{46}Ti, *b* - ^{48}Ti, *c* - ^{50}Ti isotopes. The length of the horizontal lines is proportional to the angular momentum, *J*. The experimental parity is indicated by blue for negative parity and red for positive parity. The black points show experimental spin-parity with multiple of no *Jp* assignments. (See color Figure on the journal website.)

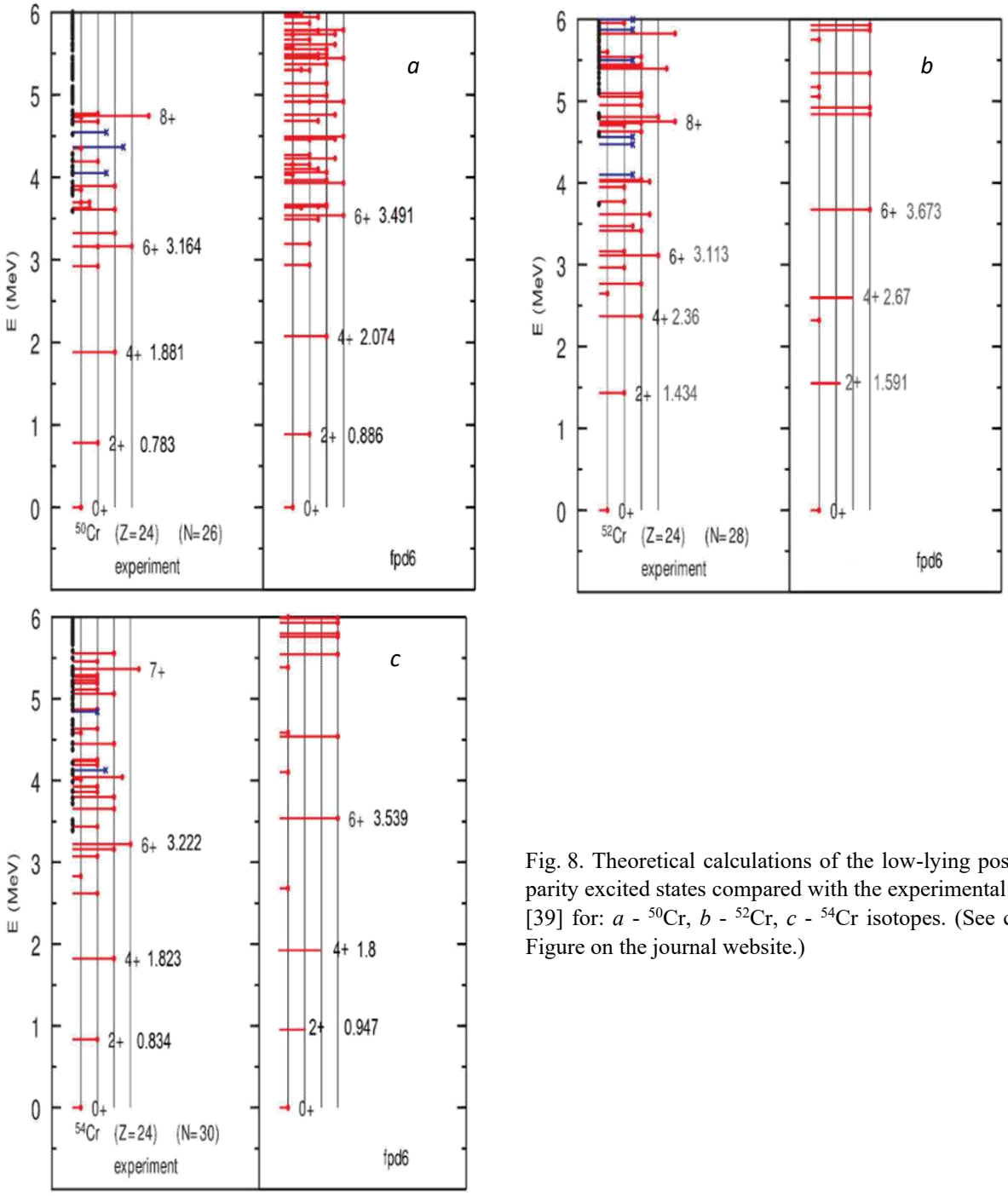

Fig. 8. Theoretical calculations of the low-lying positive parity excited states compared with the experimental data [39] for: *a* - ^{50}Cr, *b* - ^{52}Cr, *c* - ^{54}Cr isotopes. (See color Figure on the journal website.)

3.4. Quadrupole deformation

The potential energy curves (PECs) as a function of the quadrupole deformation parameter β_2 in the selected Titanium and Chromium isotopes are calculated using the HF + BCS method with Sly4 parametrizations [40]. The upper panel illustrates the density profiles of neutrons and protons in two dimensions for the axially deformed density, denoted as (*a*), representing the oblate shape. Conversely, the lower panel depicts the density profiles for the prolate shape, denoted as (*b*). The left side of the figures displays the neutron density, while the right side displays the proton density [41]. Notably, these profiles are presented for isotopes of Titanium and Chromium, corresponding to the β_2 values. For Titanium isotopes, in Figs. 9 - 11, there is only one almost spherical local minimum. We can notice that the stability increases for ^{50}Ti ($N = 28$) nucleus in Fig. 11. Furthermore, the PEC$_S$ for ^{46}Ti and ^{48}Ti isotopes have two minima, indicating the presence of a semi-spherical shape at the point of quadrupole deformation $\beta_2 = -0.051$. The corresponding PEC$_S$ for ^{46}Ti and ^{48}Ti isotopes are –388.5 and –409.8 MeV, respectively. Additionally, the prolate deformation is more pronounced in ^{46}Ti at the point of quadrupole

deformation $\beta_2 = 0.252$ with PEC_S curves equal to –389.1 MeV, compared to ^{48}Ti at the point of quadrupole deformation $\beta_2 = 0.201$ with PEC_S equal to 310 MeV.

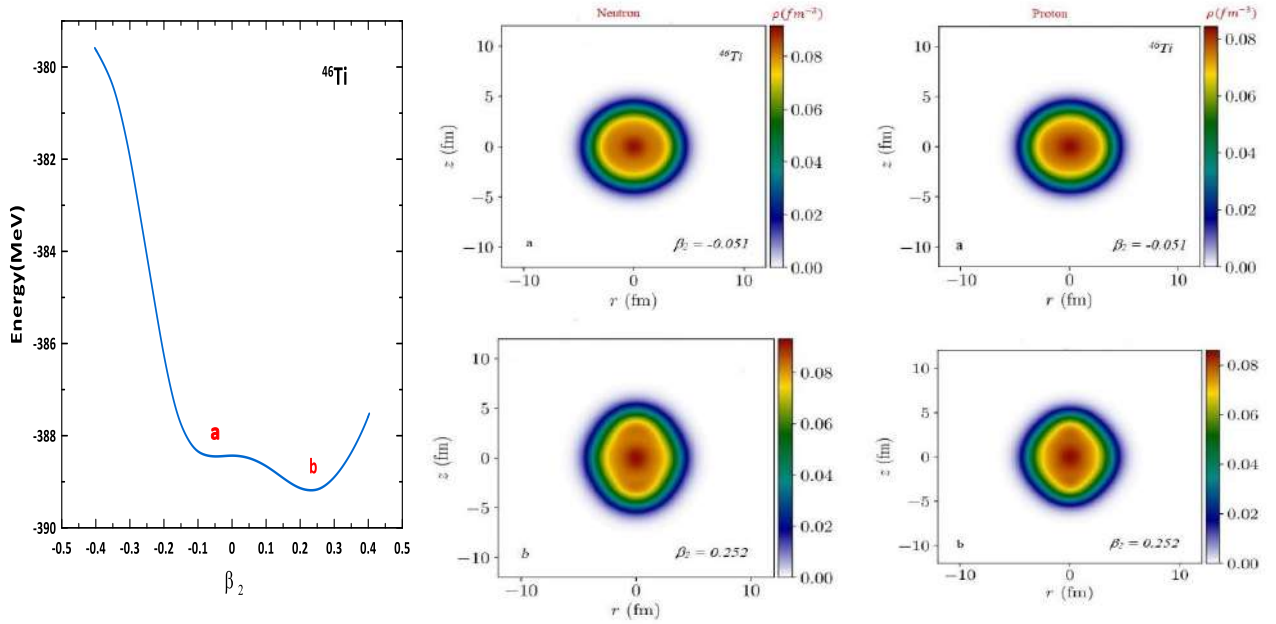

Fig. 9. The *left panel* illustrates the β_2 parameter for ^{46}Ti as a function of energy. In the *right panels*, nuclear density calculations for two deformed shapes labeled as *a* (*upper panel*) and *b* (*lower panel*) are displayed for neutrons (on the *left*) and protons (on the *right*). (See color Figure on the journal website.)

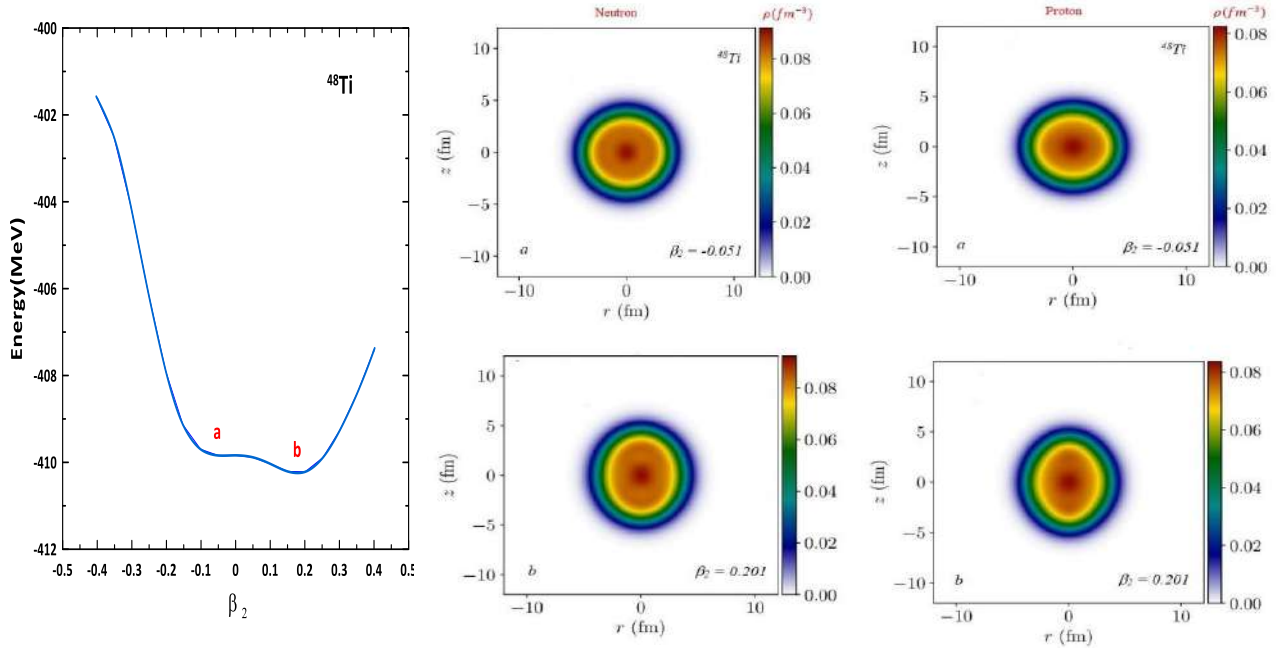

Fig. 10. The *left panel* illustrates the β_2 parameter for ^{48}Ti as a function of energy. In the *right panels*, nuclear density calculations for two deformed shapes labeled as *a* (*upper panel*) and *b* (*lower panel*) are displayed for neutrons (on the *left*) and protons (on the *right*). (See color Figure on the journal website.)

Fig. 11 unlike ^{46}Ti and ^{48}Ti, which show multiple minima corresponding to different deformed shapes, ^{50}Ti exhibits only one minimum. The spherical minima found in ^{50}Ti around the point of quadrupole deformation $\beta_2 = 0$ indicates that this nucleus has spherical shapes with potential energy surface (PES_C) equal to –433 MeV. It is important to note that the shell of the ^{50}Ti is closed at the magic number (number of neutrons equals 28). The spherical densities for both neutrons and protons confirm that the ^{50}Ti nucleus is not deformed. This lack of deformation suggests that the nuclear forces in ^{50}Ti are balanced in such a way that the nucleus maintains a spherical shape.

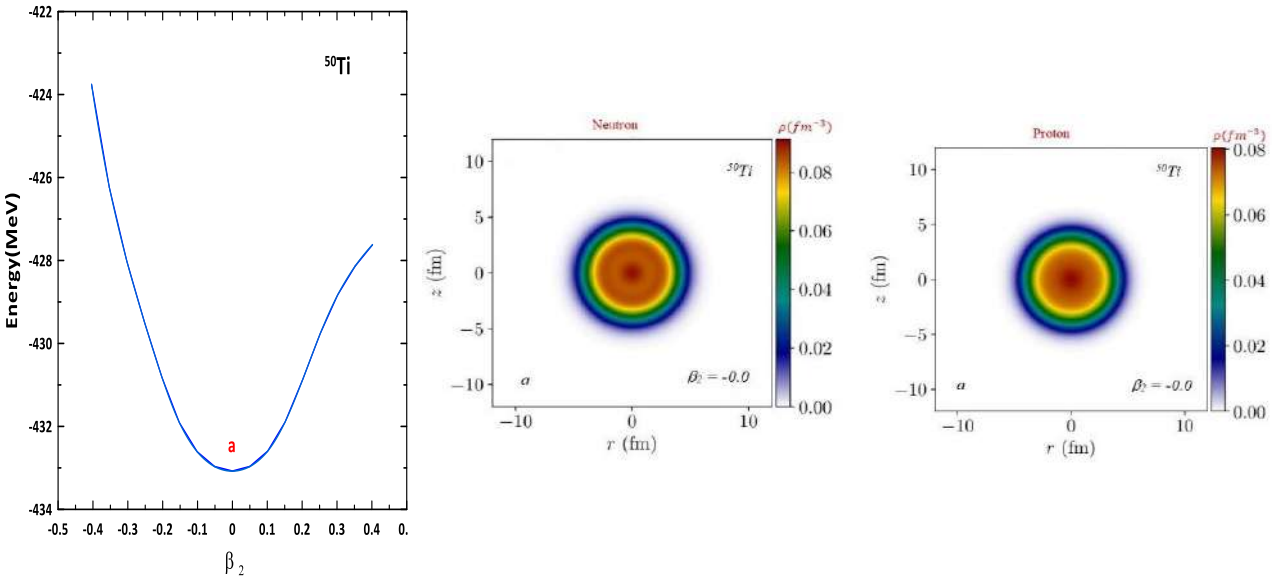

Fig. 11. The *left panel* illustrates the β_2 parameter for ^{50}Ti as a function of energy. In the *right panels*, nuclear density calculations for one deformed shape labeled as *a* for neutrons (on the *left*) and protons (on the *right*). (See color Figure on the journal website.)

As shown in Figs. 12 and 13, both exhibit complex deformation behavior with two different shapes (oblate and prolate), indicating more intricate nuclear properties. In contrast, ^{52}Cr shows higher stability in a perfectly spherical shape, reflecting an ideal balance of nuclear forces. The degree of deformation in the prolate shape is more pronounced in ^{50}Cr than in ^{54}Cr, suggesting that the deformation behavior evolves with increasing neutron number. These variations between the isotopes have significant implications for their behavior in nuclear reactions and their physical properties. The PES_C of ^{50}Cr isotope has two minimums indicating the coexistence of oblate and prolate deformations. The oblate shape is observed at a point quadrupole deformation $\beta_2 = -0.101$, where the PES_C energy of –424 MeV. On the flip side, a prolate deformation is exhibited at a point quadrupole deformation $\beta_2 = 0.251$, with the PES_C –426 MeV. Fig. 13 shows that the PES_C in ^{52}Cr, one sees that the minimum is spherical shapes at the point of quadrupole deformation β_2 value 0.0 at the PES_C equal to –446 MeV.

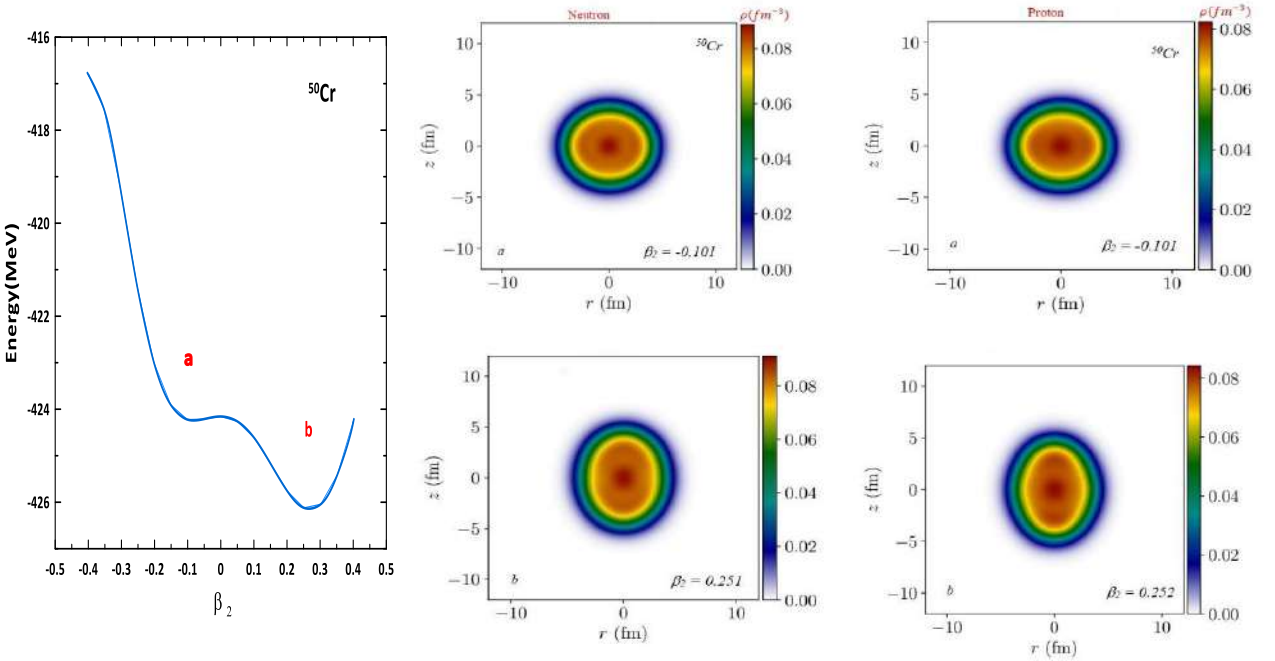

Fig. 12. The *left panel* illustrates the β_2 parameter for ^{50}Cr as a function of energy. In the *right panels*, nuclear density calculations for two deformed shapes labeled as *a* (*upper panel*) and *b* (*lower panel*) are displayed for neutrons (on the *left*) and protons (on the *right*). (See color Figure on the journal website.)

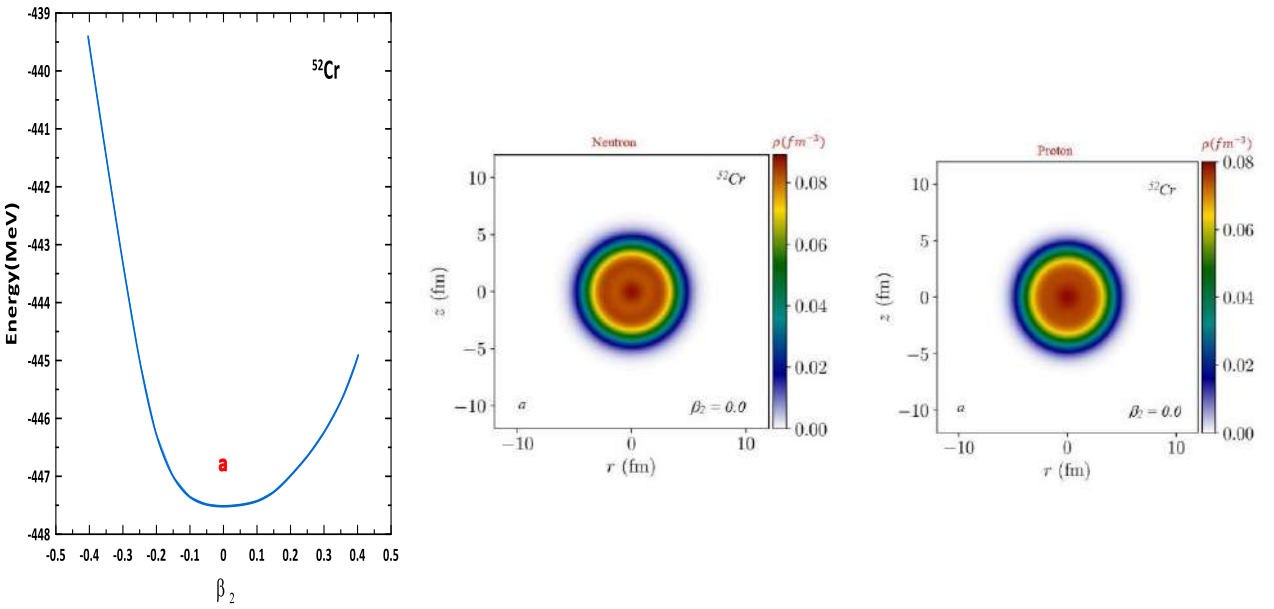

Fig. 13. The *left panel* illustrates the β_2 parameter for ^{52}Cr as a function of energy. In the *right panels*, nuclear density calculations for one deformed shape labeled as *a* are displayed for neutrons (on the *left*) and protons (on the *right*). (See color Figure on the journal website.)

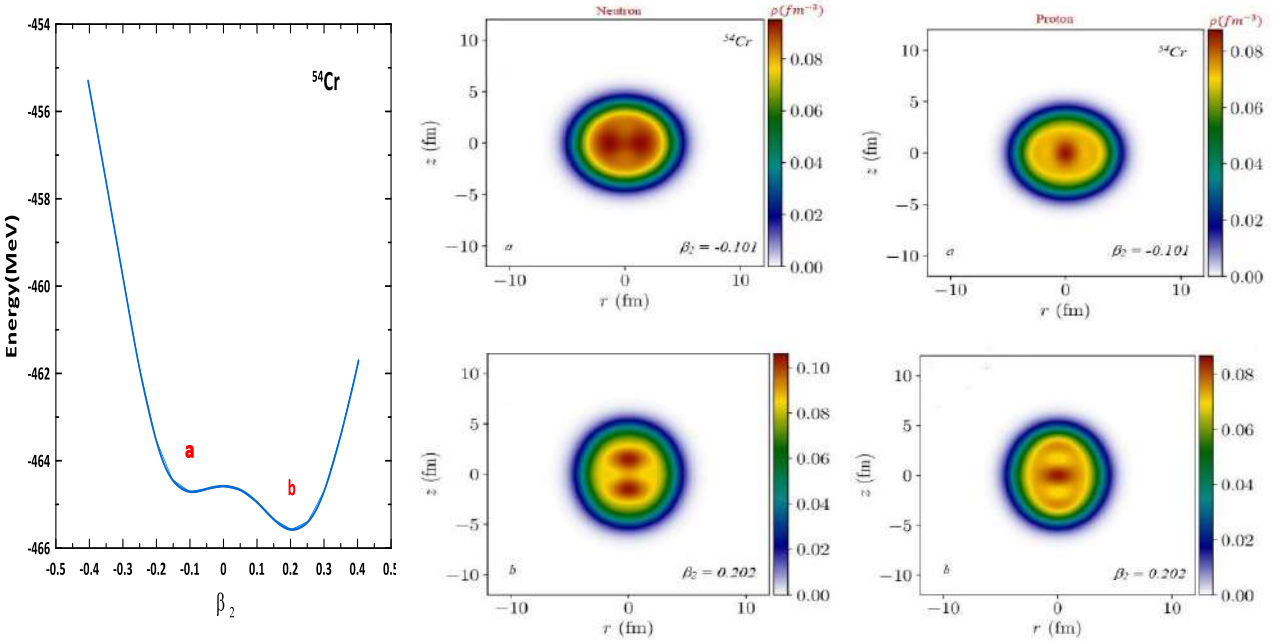

Fig. 14. The *left panel* illustrates the β_2 parameter for ^{54}Cr as a function of energy. In the *right panels*, nuclear density calculations for two deformed shapes labeled as *a* (*upper panel*) and *b* (*lower panel*) are displayed for neutrons (on the *left*) and protons (on the *right*). (See color Figure on the journal website.)

Fig. 14 shows that the PES$_C$ for ^{54}Cr has two minima, which causes prolate and oblate deformations to coexist. The oblate deformation at the point of quadrupole deformation $\beta_2 = -0.101$ at PES is equal to –465.2 MeV. Additionally, we obtain the prolate deformation value for the point of quadrupole deformation $\beta_2 = 0.251$ PESc equal to –466.3 MeV.

Table 3. **Comparison of current β_2 and BE with those from P. Möller et al. [42]**

Nucleus	β_2 equilibrium present work	β_2 equilibrium [42]	BE, MeV present work	BE, MeV [42]
^{46}Ti	0.050	0.021	389.836	399.29
^{48}Ti	0.101	0.011	412.198	420.36
^{50}Ti	0.000	0.000	433.076	438.59
^{50}Cr	0.251	0.194	429.111	435.77
^{52}Cr	0.000	0.000	451.902	457.40
^{54}Cr	0.151	0.161	469.570	473.90

Additionally, they were also compared in Table 3 with the ground state deformation values of P. Möller et al. [42], which are based on the finite-range droplet macroscopic model and the folded-Yukawa single-particle microscopic model. Examining these values shows a reasonable agreement with the data from P. Möller et al.

4. Conclusions

Our recent study delved into the nuclear deformation of specific Titanium and Chromium isotopes by employing the SM and HF approximation. This investigation yielded valuable insights into their electromagnetic properties and internal structures. The calculated μ and $Q2$ moments, in addition to inelastic longitudinal Coulomb electroexcitation form factors, have significantly contributed to a comprehensive understanding of the isotopes' electromagnetic characteristics. Our research has emphasized the impact of nuclear single-particle potentials, two-body effective interactions, and methods of computing nuclear effective charge on the behavior of inelastic form factors. These properties can effectively capture the general trends observed in experimental data in specific cases. Furthermore, our study estimated the β_2 and related nuclear density for deformed shapes using HF + BCS, shedding light on the distribution of neutrons and protons within the nuclei. This insight is crucial for comprehending the nuclear structure and validating its ability to reproduce established experimental findings.

REFERENCES

1. A. Bohr, B.R. Mottelson. *Nuclear Structure*. Vol. 1. Single-Particle Motion (New York, Benjamin, 1969).
2. K.L.G. Heyde. *The Nuclear Shell Model* (Berlin, Heidelberg, Springer-Verlag, 1994).
3. W. Greiner, J.A. Maruh. *Nuclear Models* (Berlin, Springer, 1996).
4. P. Ring, P. Schuck. *The Nuclear Many-Body Problem* (Berlin, Heidelberg, New York, Springer-Verlag, 2004) 716 p.
5. R.A. Radhi, A.A. Alzubadi, A.H. Ali. Calculations of the quadrupole moments for some nitrogen isotopes in p and psd shell model spaces using different effective charges. Iraqi J. Sci. 58 (2017) 878.
6. R.A. Radhi, A.A. Alzubadi, N.S. Manie. Electromagnetic multipoles of positive parity states in ^{27}Al by elastic and inelastic electron scattering. Nucl. Phys. A 1015 (2021) 122302.
7. G.W. Harby, A.A. Alzubadi. Calculation of the magnetic dipole and electric quadrupole moments of some sodium isotopes using shell model with Skyrme interaction. Iraqi J. Phys. 20 (2022) 40.
8. T. Otsuka et al. Evolution of shell structure in exotic nuclei. Rev. Mod. Phys. 92 (2020) 015002.
9. H. Sagawa, B.A. Brown. E2 core polarization for sd-shell single-particle states calculated with a Skyrme-type interaction. Nucl. Phys. A 430 (1984) 84.
10. G. Neyens. Nuclear magnetic and quadrupole moments for nuclear structure research on exotic nuclei. Rep. Prog. Phys. 66 (2003) 633.
11. S. Raman, C.W. Nestor, Jr., P. Tikkanen. Transition probability from the ground to the first-excited 2^+ state of even-even nuclides. Atomic Data Nucl. Data Tables 78 (2001) 1.
12. K. Yamada. Ph.D. Thesis. Department of Physics, Rikkyo University, Toshima (Tokyo, Japan, 2004).
13. G. Mukherjee, S.K. Sharma. Inelastic electron scattering form factors for the excitation of 2^+ states in some $2p$-$1f$ shell nuclei. Phys. Rev. C 29 (1984) 2101.
14. R.B.M. Mooy, P.W.M. Glaudemans. Electron scattering form factors for fp-shell nuclei. Nucl. Phys. A 438 (1985) 461.
15. R.A. Radhi, A.A. Alzubadi. Study the nuclear form factors of low-lying excited states in ^{7}Li nucleus using the shell model with Skyrme effective interaction. Few-Body Systems 60 (2019) 57.
16. A.A. Alzubadi, N.F. Latooffi, R.A. Radhi. Shell model and Hartree-Fock calculations for some exotic nuclei. Int. J. Mod. Phys. E 24 (2015) 1550099.
17. R.A. Radhi, A.A. Alzubadi, E.M. Rashed. Shell model calculations of inelastic electron scattering for positive and negative parity states in ^{19}F. Nucl. Phys. A 947 (2016) 12.
18. A.H. Ali, A.A. Alzubadi. Calculation magnetic dipole moments, electric quadrupole moments and form factors for some Ti isotopes. Phys. Scr. 95 (2020) 105306.
19. R.A. Radhi, A.A. Alzubadi, A.H. Ali. Magnetic dipole moments, electric quadrupole moments, and electron scattering form factors of neutron-rich *sd-pf* cross-shell nuclei. Phys. Rev C 97 (2018) 064312.
20. A.A. Alzubadi. Investigation of nuclear structure of $^{30\text{-}44}$S isotopes using spherical and deformed Skyrme-Hartree-Fock method. Indian J. Phys. 89 (2015) 619.
21. T. de Forest, Jr., J.D. Walecka. Electron scattering and nuclear structure. Adv. Phys. 15 (1966) 1.
22. B.A. Brown et al. Shell-model analysis of high-resolution data for elastic and inelastic electron scattering on ^{19}F. Phys. Rev. C 32 (1985) 1127.
23. A.A. Alzubadi, R.A. Allawi. Investigation of the magicity in some even-even Ca isotopes by using shell model and Hartree-Fock-Bogoliubov method. Indian J. Phys. 96 (2022) 1205.
24. A.A. Alzubadi, R.S. Obaid. Study of the nuclear deformation of some even-even isotopes using Hartree-Fock-Bogoliubov method (effect of the collective motion). Indian J. Phys. 93 (2019) 75.
25. H. Horie, K. Ogawa. Effective proton-neutron interaction and spectroscopy of the nuclei with N = 29. Prog. Theor. Phys. 46 (1971) 439.
26. R.A. Broglia, V. Zelevinsky (Eds.). *Fifty Years of Nuclear BCS. Pairing in Finite Systems* (World Scientific Publishing Co. Pte. Ltd., 2013) 693 p.

27. B.A. Brown, W.D.M. Rae. The shell-model code NuShellX@MSU. Nucl. Data Sheets 120 (2014) 115.
28. W.A. Richter et al. New effective interactions for the $0f1_p$ shell. Nucl. Phys. A 523 (1991) 325.
29. T. Iwamoto, H. Horie, A. Yokoyama. Inelastic electron scattering form factors for the excitation of the 2^+ states in the $1f_{7/2}$ nuclei. Phys. Rev. C 25 (1982) 658.
30. N.J. Stone. Table of Nuclear Magnetic Dipole and Electric Quadrupole Moments. IAEA, International Nuclear Data Committee INDC(NDS)-0658 (Vienna, Austria, Vienna International Centre, 2014) 171 p.
31. G.N. Flaiyh. Inelastic electron scattering form factors involving the second excited 2^+ level in the isotopes ^{50,54,52}Cr. Iraqi J. Phys. 13 (2015) 19.
32. G.N. Flaiyh. Core polarization effects on the inelastic longitudinal electron scattering form factors of ^{48,50}Ti and ^{52,54}Cr nuclei. Iraqi J. Sci. 57 (2016) 639.
33. J. Heisenberg, J.S. McCarthy, I. Sick. Inelastic electron scattering from several Ca, Ti and Fe isotopes. Nucl. Phys. A 164 (1971) 353.
34. L.J. Tassie. A model of nuclear shape oscillations for γ-transitions and Electron Excitation. Aust. J. Phys. 9 (1956) 407.
35. J.W. Lightbody, Jr. et al. Elastic and inelastic electron scattering from ^{50,52,54}Cr. Phys. Rev. C 27 (1983) 113.
36. P.K. Raina, S.K. Sharma. Form factors and transition charge densities for the quadrupole and hexadecupole electroexcitation of some $2p$-$1f$ shell nuclei. Phys. Rev. C 37 (1988) 1427.
37. A.M. Selig et al. Effective electro-magnetic operators of ^{50}Ti investigated with the (e, e′) reaction. Nucl. Phys. A 476 (1988) 413.
38. A. Poves et al. Shell model study of the isobaric chains A = 50, A = 51 and A = 52. Nucl. Phys. A 694 (2001) 157.
39. Live Chart of Nuclides.
40. J. Erler, P. Klüpfel, P-G. Reinhard. Self-consistent nuclear mean-field models: example Skyrme-Hartree-Fock. J. Phys. G 38 (2011) 33101.
41. A.A. Alzubadi, R.S. Obaid. An analysis of the tensor force and pairing correlation on the disappearance of nuclear magicity at N = 28 region. Braz. J. Phys. 53 (2023) 99.
42. P. Möller et al. Nuclear ground-state masses and deformations: FRDM (2012). At. Data Nucl. Data Tables 109-110 (2016) 1.

А. А. Альзубаді*, Р. Т. Махді

Фізичний факультет, Науковий коледж, Багдадський університет, Багдад, Ірак

*Відповідальний автор: ali.abdullatif@sc.uobaghdad.edu.iq

ДОСЛІДЖЕННЯ ЯДЕРНОЇ ДЕФОРМАЦІЇ ТА ПОЗДОВЖНІХ ФОРМ-ФАКТОРІВ У ДЕЯКИХ ЯДРАХ *fp*-ОБОЛОНКИ ЗА ДОПОМОГОЮ ОБОЛОНКОВОЇ МОДЕЛІ ТА НАБЛИЖЕННЯ ХАРТРІ - ФОКА

У даному дослідженні вивчалась ядерна деформація певних ізотопів титану та хрому з використанням оболонкової моделі та наближення Хартрі - Фока в модельному просторі *fp*-оболонки. Розраховано магнітні дипольні та електричні квадрупольні моменти, непружні поздовжні кулонівські форм-фактори та енергії низькоенергетичних рівнів. Одночастинкові елементи матриці густини переходу було обчислено для кожного переходу в модельному просторі *fp*-оболонки за допомогою ефективної взаємодії двох тіл FPD6. Досліджено вплив варіювання одночастинкових ядерних потенціалів, таких як гармонічний осцилятор, потенціал Вудса - Саксона та Скірма - Хартрі - Фока, порівняно з експериментальними даними. Розбіжності з експериментальними даними призводили до коригування ефективної взаємодії двох тіл або моделі розрахунку ефективного заряду ядра для конкретних переходів. Крім того, проаналізовано поверхневу потенційну енергію та розподіл ядерної густини залежно від параметра квадрупольної деформації β_2 за допомогою методу Хартрі - Фока + Бардіна - Купера - Шріффера.

Ключові слова: оболонкова модель, модельний простір *fp*-оболонки, метод Скірма - Хартрі - Фока, параметри квадрупольної деформації, наближення Хартрі - Фока + Бардіна - Купера - Шріффера.

Надійшла / Received 12.10.2024